

Article

Research on the Dynamic Control Method of CFETR Multi-Purpose Overload Robot

Congju Zuo ^{1,2,3}, Guodong Qin ¹ , Hongtao Pan ¹, Liang Xia ³, Feng Wang ³, Pucheng Zhou ³, Xiaoyan Qin ³, Ning Shi ³, Leiji Lu ³, Ruijuan Zhao ³, Chenhui Wan ⁴, Guangnan Luo ¹, Weihua Wang ^{1,5,*} and Yong Cheng ^{1,*}

¹ Institute of Plasma Physics, Chinese Academy of Sciences, Hefei 230031, China; judy@mail.ustc.edu.cn (C.Z.); gdqin@ipp.ac.cn (G.Q.); panht@ipp.ac.cn (H.P.); gnluo@ipp.ac.cn (G.L.)

² Science Island Branch of Graduate School, University of Science and Technology of China, Hefei 230026, China

³ Department of Information Engineering, Army Academy of Artillery and Air Defense, Hefei 230031, China; xialiang_815@126.com (L.X.); fengwang_1973@126.com (F.W.); zhoupc@hit.edu.cn (P.Z.); xiaoyanqin_hf@163.com (X.Q.); shining1698@126.com (N.S.); liejilu@126.com (L.L.); venus_ruijuan@126.com (R.Z.)

⁴ School of Mechanical Science and Engineering, Huazhong University of Science and Technology, Wuhan 430074, China; wanchenhui@hust.edu.cn

⁵ Institute of Physical Science and Information Technology, Anhui University, Hefei 230031, China

* Correspondence: whwang@ipp.ac.cn (W.W.); chengyong@ipp.ac.cn (Y.C.)

Abstract: The CFETR multi-purpose overload robot (CMOR) is a key subsystem of the remote handling system of the China fusion engineering test reactor (CFETR). This paper first establishes the kinematic and dynamic models of CMOR and analyzes the working process in the vacuum chamber. Based on the uncertainty of rigid-flexible coupling, a CMOR adaptive robust sliding mode controller (ARSMC) is designed based on the Hamilton-Jacobi equation to enhance the robustness of the control system. In addition, to compensate the influence of non-geometric factors on position accuracy, an error compensation method is designed. Based on the matrix differentiation method, the CMOR coupling parameter errors are decoupled, and then the gridded workspace principle is used to identify the parameter errors and improve the motion control accuracy. Finally, the CMOR rigid-flexible coupling simulation system is established by ADAMS-MATLAB/Simulink to analyze the dynamic control effect of ARSMC. The simulation results show that the CMOR end position error exceeds 0.1 m for single joint motion. The average value of CMOR end position error is less than 0.025 m after compensation, and the absolute error value is reduced by 4 times, improves the dynamic control accuracy of CMOR.

Keywords: CFETR; multi-purpose overload robot; sliding mode controller; error compensation; rigid-flexible control



Citation: Zuo, C.; Qin, G.; Pan, H.; Xia, L.; Wang, F.; Zhou, P.; Qin, X.; Shi, N.; Lu, L.; Zhao, R.; et al. Research on the Dynamic Control Method of CFETR Multi-Purpose Overload Robot. *Appl. Sci.* **2023**, *13*, 10487. <https://doi.org/10.3390/app131810487>

Academic Editor: Paolo Renna

Received: 5 July 2023

Revised: 14 September 2023

Accepted: 18 September 2023

Published: 20 September 2023



Copyright: © 2023 by the authors. Licensee MDPI, Basel, Switzerland. This article is an open access article distributed under the terms and conditions of the Creative Commons Attribution (CC BY) license (<https://creativecommons.org/licenses/by/4.0/>).

1. Introduction

Nuclear fusion energy is recognized as a clean energy source and is expected to solve the energy shortage crisis for mankind once and for all [1,2]. Since China joined ITER in 2003, Chinese scientists have been at the forefront of research on tokamak nuclear fusion devices in the world [3]. The China fusion engineering test reactor (CFETR) is a large scientific experimental device designed and developed independently by Chinese researchers [4]. It is a complex electrophysical device where the high-temperature plasma exposes the core components to a harsh environment of thermal loads, electromagnetic forces, dust contamination, and neutron irradiation during operation. Due to this extreme environment, maintenance tasks can only be performed with the help of remote handling (RH) technology [5,6]. To perform maintenance tasks in the confined environment of the fusion reactor, Oxford UK has designed a multi-purpose deployer (MPD) based on the remote handling tasks of the ITER vacuum chamber [7–9]. The remote handling robot team

at the Institute of Plasma Physics, CAS, has designed a CFETR multi-purpose overload robot (CMOR) based on the MPD to address the need for refined maintenance of CFETR core components. CMOR adopts a long cantilever hinged structure, the long robot arm with 9 degrees of freedom end load 2 tons, the short robot arm with 7 degrees of freedom end load 2.5 tons, position accuracy ± 10 mm, maximum speed 100 mm/s. The CMOR redundant degree of freedom design can circumvent the physical limits of joints [10] surrounding obstacles [11] and motion singularities [12] to meet the requirement of full coverage of the vacuum chamber with “D” shaped cross section. Due to the rigid-flexible coupling deformation, the static deformation error of CMOR reaches 77 mm [13,14], which makes accurate dynamic control very difficult.

CMOR is a typical multi-body dynamical system, and the most commonly used dynamical modelling methods are the Lagrange equation, Newton-Euler equation, graph theory method, Kane method and variational method [15]. CMOR belongs to the flexible multi-body system with small deformation, mainly joint flexibility and link flexibility causing the structural deformation of the robot arm. The main methods for modelling CMOR flexible links are the finite element method, the hypothetical modal method and the centralized parameter method [16,17]. Al-Bedoor et al. used the finite element method to model the flexibility of a robot with moving joints [18,19]. Subudhi et al. used the hypothetical modal method to model the flexibility of the robotic arm linkage to achieve accurate control of the robotic arm [20]. Zhu et al. used a centralized parametric method to model flexible links and achieve real-time control of the end trajectory of the robot arm [21]. Braganza et al. designed a robot controller using a neural network feedforward to compensate for kinetic uncertainty [22]. To optimize the kinematic constraints of the robot, Racioppo et al. designed a robot control scheme combining obstacle interaction and path tracking [23]. Goldman et al. proposed a motion control algorithm for a robot in an unknown contact environment and analyzed the mapping relationship of the spatial torques of the robot joints [24]. Ider et al. modelled the flexible joint of a robotic arm equivalent to a torsion spring, damped system [25]. Khalil et al. described the flexible joint by second-order time-varying equations and used the input and output parameters of the system to build an equivalent model of the flexible system [26]. For the problem of controller design for nonlinear, parameter uncertain systems, scholars have proposed a variety of advanced control techniques, including robust control techniques, sliding mode control techniques, adaptive control and neural network techniques [27]. Sliding mode control and adaptive control have outstanding advantages and are robust against system uncertainty and external disturbances [28]. Roy et al. designed a new adaptive sliding mode controller to reduce the sliding mode surface oscillations and improve the robustness of the robot under various practical uncertainty conditions [29]. For the parameter error compensation problem, Li et al. used a genetic particle swarm algorithm to optimize a neural network prediction error model to achieve the compensation of target points in the whole workspace of the robot [30]. Le et al. constructed an artificial neural network that can simultaneously identify the robot's kinematic and flexibility parameters to compensate for the unmodeled error [31–33]. Zhou et al. compensated the joint flexibility error by modeling the geometric and flexibility errors [34].

The research and application of CMOR are still in the exploration stage, and its precise operation control problem is an urgent challenge to be solved. The structural characteristics of CMOR with a large slenderness ratio and large load working conditions make the deformation error and control error of CMOR flexible joint and flexible link larger. In this paper, the kinematic and dynamic models of CMOR are first established and the working process of CMOR is analyzed. For the CMOR model uncertainty and external disturbance problems, an adaptive robust sliding mode controller (ARSMC) is designed for dynamic control of CMOR by combining the sliding mode control and Hamilton Jacobi equation. Then a position error compensation method is designed to further improve the CMOR position accuracy through workspace gridding. Finally, a co-simulation system of CMOR is established using ADAMS 2013 and MATLAB 2017b/Simulink software to

verify the effectiveness of the dynamic control accuracy. Considering the above study, this paper is divided into 5 sections. Section 2 analyzes the working process of CMOR in the vacuum chamber and establishes the kinematic and dynamic models. Section 3 designs the ARSMC controller and proposes a gridded variable parameter error compensation method. Section 4 develops a CMOR simulation model and analyzes the control effects. Finally, conclusions are given in Section 5.

2. CMOR Modelling

2.1. Kinematic Modelling

CMOR is a multi-degree-of-freedom robotic system for the maintenance of internal components of CFETR vacuum chambers [35]. It consists of CASK parts transfer vehicle, CMOR robot arm body, multifunctional toolbox, and CMOR end-effectors as shown in Figure 1. To describe the motion of the CMOR, the first step requires accurate modelling of the kinematics of the CMOR. In this paper, the improved DH parameter method is used to model the forward kinematics of CMOR, and the range of DH parameters and joint variables of each link are taken as shown in Table 1. The kinematic relationship between two adjacent links of CMOR is

$${}^{i-1}T_i = \begin{bmatrix} c\theta_i & -s\theta_i c\alpha_i & s\theta_i s\alpha_i & a_i c\theta_i \\ s\theta_i & c\theta_i c\alpha_i & -c\theta_i s\alpha_i & a_i s\theta_i \\ 0 & c\alpha_i & s\alpha_i & d_i \\ 0 & 0 & 0 & 1 \end{bmatrix} \tag{1}$$

where c denotes \cos , s denotes \sin , a_i is the linkage length, α_i is the joint torsion angle deviation, d_i is the linkage deflection, and θ_i is the joint rotation angle. To eliminate the singularity problem arising from the mutual parallelism between the two axes of CMOR joint 1 joint 2, the rotation R_i is introduced to modify the DH model as follows:

$$R_i = \begin{bmatrix} c\beta_i & 0 & s\beta_i & 0 \\ 0 & 1 & 0 & 0 \\ -s\beta_i & 0 & c\beta_i & 0 \\ 0 & 0 & 0 & 1 \end{bmatrix} \tag{2}$$

The CMOR kinematic model is established using the modified DH parameters, and the homogeneous coordinate transformation matrix between adjacent links is

$${}^{i-1}T_i = \text{Rot}(X, \alpha_{i-1})\text{Trans}(X, a_{i-1})\text{Rot}(Z, \theta_{i-1})\text{Trans}(Z, d_i)\text{Rot}(Y, \beta_i) = \begin{bmatrix} c\theta_i c\beta_i - s\theta_i s\alpha_i s\beta_i & -s\theta_i c\alpha_i & c\theta_i c\beta_i - s\theta_i s\alpha_i s\beta_i & a_i c\theta_i \\ s\theta_i c\beta_i + c\theta_i s\alpha_i s\beta_i & c\theta_i c\alpha_i & c\theta_i c\beta_i - s\theta_i s\alpha_i s\beta_i & a_i s\theta_i \\ -c\alpha_i s\beta_i & s\alpha_i & c\alpha_i c\beta_i & d_i \\ 0 & 0 & 0 & 1 \end{bmatrix} \tag{3}$$

where $\theta_i, a_i, \alpha_i, d_i, \beta_i$ are the DH parameters of the CMOR joint coordinate system.

Then the position relationship of the CMOR end-effector concerning the base coordinate system can be expressed as

$${}^0_8T = {}^0_1T R_2 {}^1_2T {}^2_3T \cdots {}^6_7T {}^7_8T \tag{4}$$

where 0_8T denotes the position of the CMOR end-effector with respect to the base coordinate system and R_2 denotes the rotation matrix around the Y-axis introduced by avoiding singularities when joints J_1 and J_2 are parallel.

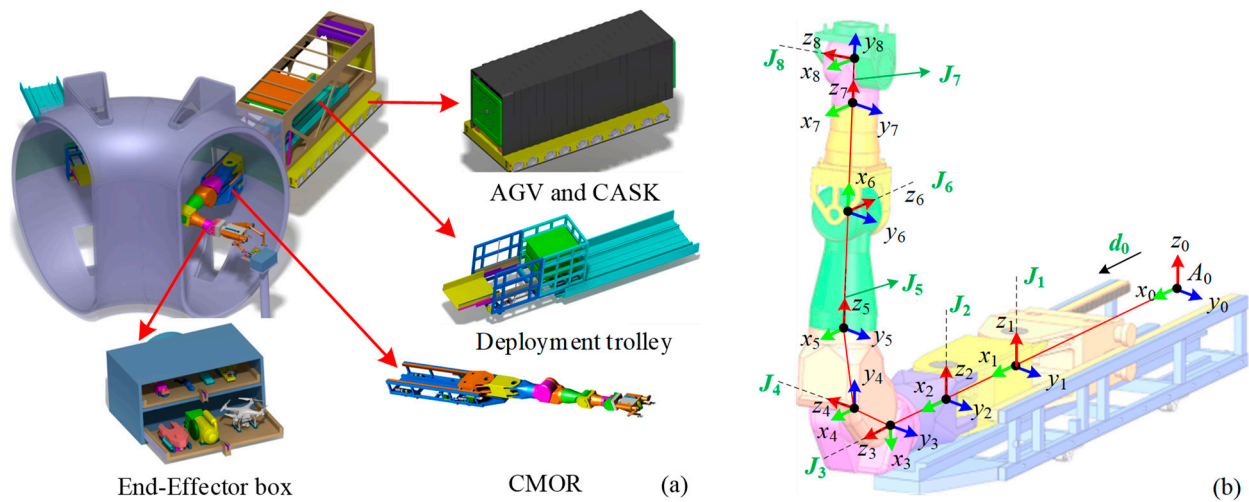


Figure 1. Composition of CFETR multipurpose overload robot system (a) Components of the CMOR remote handling system (b) Coordinate system of CMOR.

Table 1. CMOR improved DH parameters.

Link i	Variable θ_i	Rotation Angle ($^\circ$)	Distance (m)	Range ($^\circ$)
1	θ_1	(0, 0, 0)	(0, 0, 0)	$-90 \sim +90^\circ$
2	θ_2	(0, 0, 0)	(1.76, 0, 0)	$-90 \sim +90^\circ$
3	θ_3	(0, 90° , 0)	(1.33, 0, 0)	$-180 \sim +180^\circ$
4	θ_4	(90° , 0, 90°)	(-0.38, 0, 0.91)	$0 \sim +180^\circ$
5	θ_5	(-90° , 0, 0)	(0.38, 0.94, 0)	$-180 \sim +180^\circ$
6	θ_6	(0, -90° , 0)	(0, 0, 1.3)	$-90 \sim +90^\circ$
7	θ_7	(0, 90° , 0)	(1.19, 0, 0)	$-100 \sim +100^\circ$
8	θ_8	(90° , 0, 0)	(0, 0, 0.46)	$-90 \sim +90^\circ$

2.2. CMOR Work Process Analysis

The CMOR is first mounted and stored in a folded position on the mobile platform of the CASK parts transfer vehicle during shutdown as shown Figure 2a. During operation, the CMOR and the end-effectors are transported together in a CASK parts transfer vehicle to the maintenance port of the fusion reactor vacuum chamber as shown in Figure 2b. The CMOR transporter will be connected to the middle part of the vacuum chamber and locked by a locking mechanism, as shown in Figure 2c. Then, the shield door is opened and the CMOR is transported together with the end-effector through the moving platform to the inside of the vacuum chamber as shown in Figure 2d,e. The CMOR is controlled by trajectory planning, trajectory tracking, and master-slave remote operation to reach the precise target location in the vacuum chamber to complete the work task as shown in Figure 2f. Finally, the CMOR exits the vacuum chamber maintenance port through the CASK component transfer vehicle and closes the shield door to complete the entire operation.

CMOR mainly adopts the working mode of the macro-micro robotic arm, i.e., CMOR and end-effectors. Different maintenance tools are installed at the end of the CMOR to complete the specified maintenance tasks. The CMOR multifunctional toolbox generally contains: end dual arms, endoscopic inspection equipment, cutting tools, grinding tools, etc. CMOR selects specific tools in the multifunctional toolbox to perform different maintenance tasks on the core components such as quick removal and replacement of modular components of the blankets and divertors, first wall dust detection and removal, vacuum chamber inspection observation and other tasks, as shown in Figure 3.

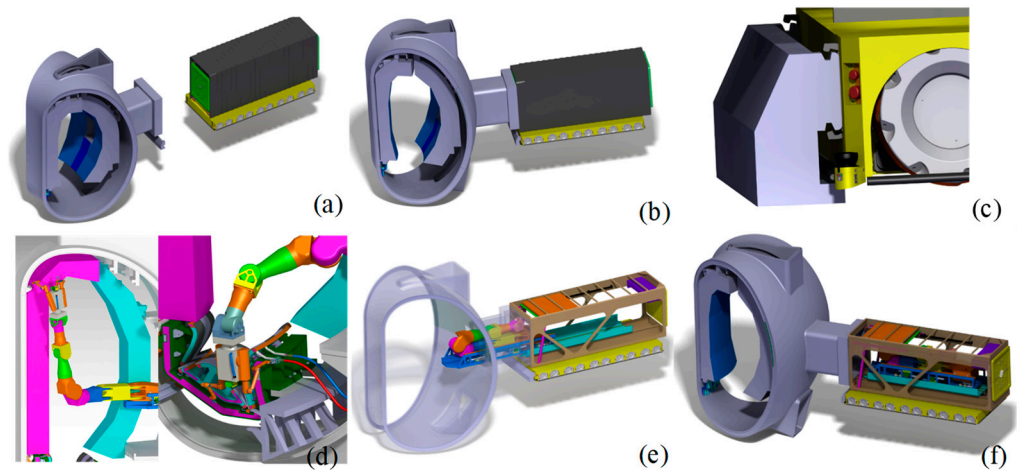


Figure 2. The working process of the CMOR system (a) CMOR installed in CASK transport vehicle (b) CMOR transport to the middle port of the vacuum chamber (c) CMOR is locked with the middle port (d) Open the screen doors (e) CMOR transport to vacuum chamber via the mobile platform (f) CMOR completes maintenance tasks on top and bottom of the vacuum chamber.

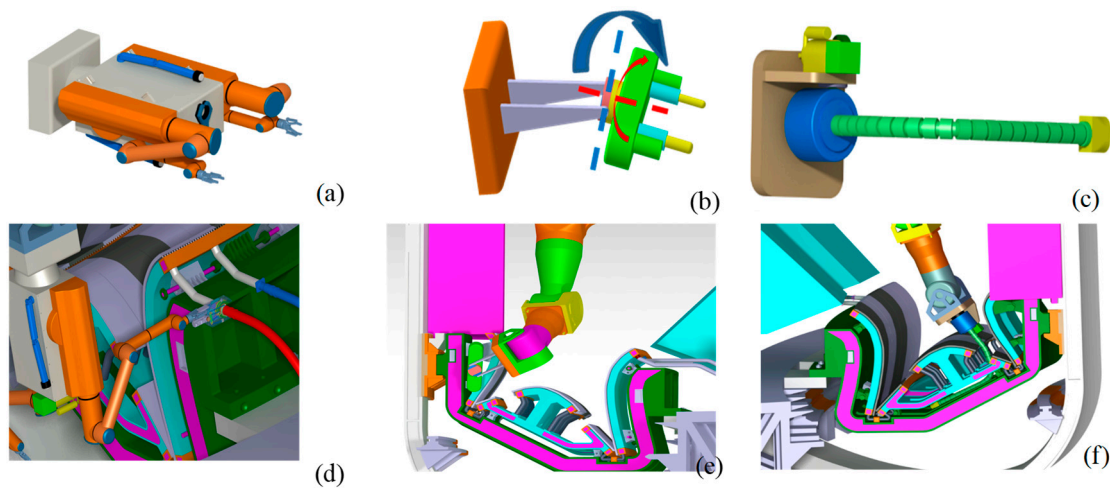


Figure 3. CMOR remote handling maintenance tasks (a) Dual arm end-effector (b) First wall target plate removal tool (c) Multi-joint endoscopic robotic arm (d) Vacuum chamber pipe cutting (e) First wall target plate removal (f) Endoscopic inspection of the bottom of the divertor.

2.3. CMOR Dynamics Model

CMOR can withstand high loads for the maintenance of vacuum chamber components. The CMOR structure with 8 degrees of freedom as shown in Figure 1b can flexibly adjust its attitude in a limited space to transport the end-effector to any maintenance location within the vacuum chamber. The end-effector has multiple degrees of freedom and is capable of performing a variety of maintenance operations. The CMOR dynamics equations are established by the Lagrangian method. The first step is to calculate the CMOR kinetic energy including the link dynamic energy K_l , the drive motor rotor kinetic energy K_r , and the load kinetic energy K_p . Therefore, the total CMOR kinetic energy is

$$K = K_r + K_l + K_p + \Delta T \tag{5}$$

where ΔT is the calculated error under unknown disturbance.

$$K_r = \frac{1}{2} \dot{\theta}^T I_a \dot{\theta} = \frac{1}{2} (N\dot{q}) I_a (N\dot{q}) = \frac{1}{2} \sum_{i=1}^8 N_i^2 \dot{q}_i^2 I_{ai} \tag{6}$$

where I_{ai} is the equivalent rotational inertia of the i -th joint actuator. \dot{q}_i is the velocity of joint i . Assume that the mass of any mass point P on joint i is dm , then its kinetic energy is

$$dk_i = \frac{1}{2}v_p^2 dm = \frac{1}{2}Trace[\sum_{j=1}^i \sum_{k=1}^i \frac{\partial T_i}{\partial q_j} r_p^i (r_p^i)^T (\frac{\partial T_i}{\partial q_k}) \dot{q}_j \dot{q}_k] dm \tag{7}$$

where T_i is the i -th joint transformation matrix, including rotation and translation transformations, and r_p^i is the position vector of the local coordinate system (relative to joint i). The kinetic energy of joint i can be obtained by integrating the kinetic energy of the mass points on joint

$$K_i = \int_{link_i} dk_i = \frac{1}{2}Trace[\sum_{j=1}^i \sum_{k=1}^i \frac{\partial T_i}{\partial q_j} (\int_{link_i} r_p^i (r_p^i)^T dm) (\frac{\partial T_i}{\partial q_k}) \dot{q}_j \dot{q}_k] \tag{8}$$

Thus, the total kinetic energy of each link in the CMOR can be written as follows

$$K_l = \sum_{i=1}^8 K_i = \frac{1}{2} \sum_{i=1}^8 Trace[\sum_{j=1}^i \sum_{k=1}^i \frac{\partial T_i}{\partial q_j} I_i (\frac{\partial T_i}{\partial q_k}) \dot{q}_j \dot{q}_k] \tag{9}$$

where I denotes the pseudo-inertia matrix expressed as follows

$$I_i = \int_{link_i} r^i (r^i)^T dm = \begin{bmatrix} \int_i x_i^2 dm & \int_i x_i y_i dm & \int_i x_i z_i dm & \int_i x_i dm \\ \int_i x_i y_i dm & \int_i y_i^2 dm & \int_i y_i z_i dm & \int_i y_i dm \\ \int_i x_i z_i dm & \int_i y_i z_i dm & \int_i z_i^2 dm & \int_i z_i dm \\ \int_i x_i dm & \int_i y_i dm & \int_i z_i dm & \int_i dm \end{bmatrix} \tag{10}$$

The CMOR load is the self-weight of the end-effector and load weight. It is assumed that all external loads are concentrated at one point on the end joint of the CMOR, so that the end load has only translational energy and no rotational energy

$$K_p = \frac{1}{2} m_p Trace[\sum_{j=1}^8 \sum_{k=1}^8 \frac{\partial T_8}{\partial q_j} r_8 r_8^T (\frac{\partial T_8}{\partial q_k}) \dot{q}_j \dot{q}_k] \tag{11}$$

where m_p is the mass of the end-effector and the load.

The second step calculates the CMOR potential energy. CMOR potential energy is mainly the link gravitational potential energy P_{gl} , joint rotor gravitational potential energy P_{gr} , and end-effector and load gravitational potential energy P_{gp}

$$P = P_{gl} + P_{gr} + P_{gp} + \Delta P \tag{12}$$

where ΔP is the potential energy calculation error. The gravitational potential energy at position r^i on any link i of the CMOR is

$${}^0_8 T = {}^0_1 T R_2 {}^1_2 T {}^2_3 T \dots {}^6_7 T {}^7_8 T \tag{13}$$

where $g^T = [0 \ 0 \ 9.81 \ 1]^T$. Integrating Equation (13), the total potential energy of each link of CMOR is obtained as

$$P_{gl} = \sum_{i=1}^8 -g^T T_i \int_{link_i} r^i dm = -\sum_{i=1}^8 m_{gi} g^T T_i r_i^i \tag{14}$$

where m_{gi} is the mass of joint i and r_i^i is the centre of gravity of joint i concerning the front joint coordinate system. CMOR rotor gravitational potential energy of any joint i

$$P_{gr} = \sum_{i=1}^8 -m_{ri} g^T T_i r_r^i \tag{15}$$

where m_{ri} is the joint i rotor mass and r_r^i denotes the rotor centre of mass concerning the joint i coordinates. The gravitational potential energy of the loaded mass of the CMOR end-effector is

$$P_{gp} = -m_{gp}g^T T_8 r_g^8 \tag{16}$$

where m_{gp} is the total mass of the end-effector and the load, and r_g^8 represents the coordinates of the load position relative to the end joint. The third step derives the CMOR dynamic equations. CMOR is a typical serial multi-joint robotic arm and the final dynamics model can be expressed as

$$T = M(q)\ddot{q} + H(q, \dot{q})\dot{q} + G(q) + D \tag{17}$$

where $\ddot{q} \in R^8$ is the acceleration vector, $\dot{q} \in R^8$ is the velocity vector, $T \in R^8$ is the torque vector, $M(q) \in R^{8 \times 8}$ is the inertial force matrix, $H(q, \dot{q}) \in R^{8 \times 8}$ is the centrifugal and Gauchy force matrix, $G(q) \in R^8$ is the gravity vector, and D denotes the bounded unknown perturbation. The torque of any joint p in Equation (17) is calculated using the Lagrangian equation as

$$\begin{aligned} T_p = & \frac{d}{dt} \frac{\partial L}{\partial \dot{q}_p} - \frac{\partial L}{\partial q_p} = N_p^2 I_{ai} \ddot{q}_p + \sum_{i=p}^8 \sum_{k=1}^i \text{Trace} \left(\frac{\partial T_i}{\partial q_k} I_i \frac{\partial T_i^T}{\partial q_p} \right) \ddot{q}_k \\ & + \sum_{i=p}^8 \sum_{j=1}^i \sum_{k=1}^i \text{Trace} \left(\frac{\partial^2 T_i}{\partial q_j \partial q_k} I_i \frac{\partial T_i^T}{\partial q_p} \right) \dot{q}_j \dot{q}_k + m_p \sum_{j=p}^8 \text{Trace} \left[\frac{\partial T_8}{\partial q_j} r_p^8 \right. \\ & \left. \left(r_p^8 \right)^T \left(\frac{\partial T_8}{\partial q_k} \right) \right] \ddot{q}_j + m_p \sum_{j=p}^8 \sum_{k=p}^8 \text{Trace} \left[\frac{\partial T_8}{\partial q_j} r_p^8 \left(r_p^8 \right)^T \left(\frac{\partial T_8}{\partial q_p} \right) \right] \dot{q}_j \dot{q}_k \\ & - \sum_{i=p}^8 m_i^s g^T \frac{\partial T_i}{\partial q_p} r_i^i - \sum_{i=p}^8 m_i^r g^T \frac{\partial T_i}{\partial q_p} r_r^i - m_p^s g^T \frac{\partial T_8}{\partial q_p} r_g^8 \\ & - K_p \left(q_p^l - q_p \right) \end{aligned} \tag{18}$$

where the Lagrangian function L is

$$\begin{aligned} L = & K - P \\ = & \frac{1}{2} \sum_{i=1}^8 N_i^2 \dot{q}_i^2 I_{ai} + \frac{1}{2} \sum_{i=1}^8 \sum_{j=1}^i \sum_{k=1}^i \text{Trace} \left(\frac{\partial T_i}{\partial q_j} I_i \frac{\partial T_i^T}{\partial q_k} \right) \dot{q}_j \dot{q}_k \\ & + \frac{1}{2} m_p \text{Trace} \left[\sum_{j=1}^8 \sum_{k=1}^8 \frac{\partial T_8}{\partial q_j} r_8 \left(r_8 \right)^T \left(\frac{\partial T_8}{\partial q_k} \right) \dot{q}_j \dot{q}_k \right] + \frac{1}{2} \sum_{i=1}^8 K_i \left(q_i^l - q_i \right)^2 \\ & + \sum_{i=1}^8 m_{gi} g^T T_i r_i^i + \sum_{i=1}^8 m_{ri} g^T T_i r_r^i + m_p^s g^T T_8 r_g^8 \end{aligned} \tag{19}$$

3. CMOR Dynamic Control Method

3.1. CMOR Closed-Loop Control Strategy

From Equation (17) the dynamics equation of the 8-joint robotic arm of CMOR can be expressed as

$$T = M(q)\ddot{q} + V(q, \dot{q})\dot{q} + G(q) + \Delta(q, \dot{q}) + dt \tag{20}$$

where $\Delta(q, \dot{q})$ is the modeling uncertainty part and dt is the bounded unknown perturbation. The ideal position command is q_d , the tracking error is $e = q - q_d$, and the design control law is

$$T = u + M(q)\ddot{q} + V(q, \dot{q})\dot{q} + G(q) \tag{21}$$

where u is the feedback control law. Taking Equation (20) into the CMOR dynamics model Equation (20) gives

$$u = M(q)\ddot{e} + V(q, \dot{q})\dot{e} + d \tag{22}$$

where $\ddot{e} = \ddot{q} - \ddot{q}_d$, $\dot{e} = \dot{q} - \dot{q}_d$, $d = \Delta(q, \dot{q}) + dt$. Define the sliding mode function as

$$s = \dot{e} + ce \tag{23}$$

where $c > 0$. Bringing Equation (23) into Equation (22) gives

$$\begin{cases} \dot{e} = s - ce \\ M\dot{s} = -Vs + \omega - d + u \end{cases} \quad (24)$$

The sliding mode allows the feedback control law u to be designed according to demand, and the sliding mode motion of the system is independent of the parameter changes of the control object and the external disturbances of the system. Therefore, the robustness of the sliding mode variable structure control system is stronger than that of the general conventional continuous system. However, the sliding-mode variable-structure control is by nature discontinuous switching characteristics, which makes the variable-structure control generate high-frequency vibration in the sliding mode, affecting the accuracy of control, increasing energy consumption, generating oscillation or instability, and damaging controller components.

Adaptive control is a control method that can modify its characteristics to adapt to changes in the dynamic characteristics of objects and disturbances. The combination of adaptive control and sliding mode variable structure control can solve the parameter uncertainty and time-varying parameter system control problems, increase the system robustness and achieve a very good control system performance.

To improve the robustness of the CMOR control system and enhance the stability of the control system under uncertainty random error parameter uptake, this paper designs an adaptive robust sliding mode controller (ARSMC) for CMOR based on the Hamilton Jacobi equation to enhance the immunity to disturbances, as shown in Figure 4. Consider the following system model

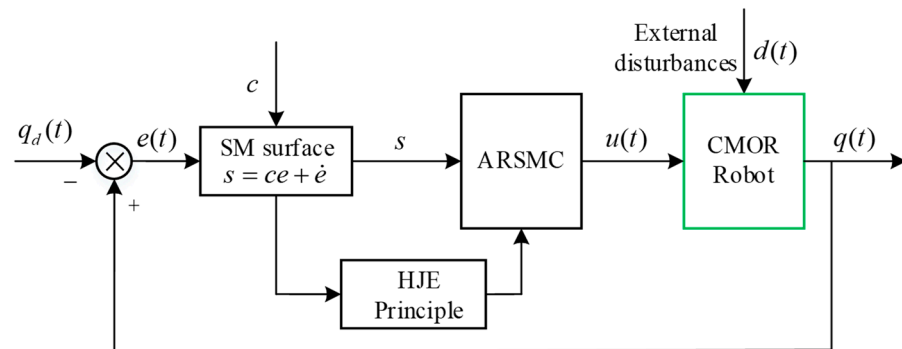


Figure 4. CMOR adaptive robust sliding mode control principle.

$$\begin{cases} \dot{x} = f(x) + g(x)d \\ z = h(x) \end{cases} \quad (25)$$

where d is the disturbance and z is the evaluation signal of the system. To achieve the adaptive robust control requirement of the CMOR system, the evaluation signal of the sliding mode function is defined as

$$z = s = \dot{e} + ce \quad (26)$$

where $c > 0$. Define the 2-Norm for modelling uncertainty and position perturbation d as

$$\|d\|_2 = \left\{ \int_0^\infty d^T d dt \right\}^{\frac{1}{2}} \quad (27)$$

To express the robustness of the system against interference, the following performance indicators are defined

$$J = \sup_{\|d\| \neq 0} \frac{\|z\|_2}{\|d\|_2} \quad (28)$$

where J is the gain of the system $\|d\|_2$, and the smaller the value of J , the better the robust performance of the system. The Hamilton Jacobi equation [36–38] can be described as follows: for any given positive real number γ , if there exists a positive definite and differentiable function $L(x) \geq 0$ and for any interfering signal d satisfying

$$\dot{L} \leq \frac{1}{2} \{ \gamma^2 \|d\|^2 - \|z\|^2 \} \tag{29}$$

Then we can obtain $J \leq \gamma$. To take advantage of the Hamilton Jacobi equation principle, Equation (24) is rewritten in the following form

$$\begin{cases} \dot{x} = f(x) + g(x)d \\ z = \dot{e} + ce \end{cases} \tag{30}$$

where $f(x) = \begin{bmatrix} s - ce \\ \frac{1}{M}(-Vs + \omega + u) \end{bmatrix}$ and $g(x) = \begin{bmatrix} 0 \\ -\frac{1}{M} \end{bmatrix}$. For the CMOR closed-loop dynamical system satisfying the restriction $J \leq \gamma$, the following control law can be obtained

$$u = -\omega - \frac{1}{2\gamma^2}s - \frac{1}{2}s \tag{31}$$

The stability of the control law is proved as follows, defining the Lyapunov function as

$$L = \frac{1}{2}s^T Ms \tag{32}$$

Then

$$\begin{aligned} \dot{L} &= s^T \dot{M}s + \frac{1}{2}s^T \dot{M}s = s^T (-Vs + \omega - d + u) + \frac{1}{2}s^T \dot{M}s \\ &= s^T \left(-d - \frac{1}{2\gamma^2}s - \frac{1}{2}s \right) + \frac{1}{2}s^T (\dot{M} - 2V)s \\ &= -s^T d - \frac{1}{2\gamma^2}s^T s - \frac{1}{2}s^T s \end{aligned} \tag{33}$$

Define

$$Q = \dot{L} - \frac{1}{2}\gamma^2 \|d\|^2 + \frac{1}{2}\|z\|^2 \tag{34}$$

Then

$$Q = -s^T d - \frac{1}{2\gamma^2}s^T s - \frac{1}{2}s^T s - \frac{1}{2}\gamma^2 \|d\|^2 + \frac{1}{2}\|z\|^2 \tag{35}$$

Since

$$-s^T d - \frac{1}{2\gamma^2}s^T s - \frac{1}{2}\gamma^2 \|d\|^2 = -\frac{1}{2} \left\| \frac{1}{\gamma}s + \gamma d \right\|^2 \leq 0 \tag{36}$$

$$-\frac{1}{2}s^T s + \frac{1}{2}\|z\|^2 = 0 \tag{37}$$

Therefore $Q \leq 0$, i.e.,

$$\dot{L} \leq \frac{1}{2}\gamma^2 \|d\|^2 - \frac{1}{2}\|z\|^2 \tag{38}$$

From the Hamilton Jacobi equation, the control law designed for the CMOR satisfies the robustness condition that $J \leq \gamma$ and the control system is stable.

3.2. CMOR Position Error Compensation Method

The parameter errors of CMOR are not uniformly distributed in the joint space due to the influence of linkage flexibility, joint flexibility, self-weight, load and motor control. For the error of each joint parameter of CMOR, the full differentiation of the coordinate transformation between adjacent links according to the differential transformation method can be obtained

$$\Delta_i^{i-1} T = \frac{\partial_i^{i-1} T}{\partial \theta} \Delta \theta + \frac{\partial_i^{i-1} T}{\partial \alpha} \Delta \alpha + \frac{\partial_i^{i-1} T}{\partial d} \Delta d + \frac{\partial_i^{i-1} T}{\partial a} \Delta a + \frac{\partial_i^{i-1} T}{\partial \beta} \Delta \beta = {}_i^{i-1} T \Delta i \tag{39}$$

where $\Delta\theta_i$ is the joint rotation angle deviation, $\Delta\alpha_i$ joint torsion angle deviation, Δd_i linkage offset deviation, Δa_i link length deviation, $\Delta\beta_i$ is the deviation of parameter β_i , $\Delta_i^{i-1}T$ is the homogeneous transformation error of adjacent links, Δ_i is the differential transformation error between adjacent linkage coordinate systems.

Due to the errors in the CMOR joint parameters, the homogeneous transformation matrix of the end coordinate system with respect to the base coordinate system is

$$T_n^0 + dT_n^0 = \left({}^0_1T + \Delta_1^0T \right) \left({}^1_2T + \Delta_2^1T \right) \cdots \left({}^{n-2}_{n-1}T + \Delta_{n-1}^{n-2}T \right) \left({}^{n-1}_nT + \Delta_n^{n-1}T \right) \quad (40)$$

where T_n^0 is the positional matrix of the CMOR end-effector coordinates to the base coordinate system, and dT_n^0 is the error matrix of the end coordinate system with respect to the base coordinate system. The above equation is rounded off by the higher-order regression term [39], and the linearized CMOR end space position error model is obtained as

$$\begin{aligned} dT_n^0 &= \sum_{i=1}^n \left[{}^0_1T \cdots {}^{i-2}_{i-1}T d \left({}^{i-1}_i T \right) {}^i_{i+1}T \cdots {}^{n-1}_nT \right] \\ &= \sum_{i=1}^n \left[{}^0_{i-1}T d \left({}^{i-1}_i T \right) {}^i_{i+1}T \cdots {}^{n-1}_nT \right] \end{aligned} \quad (41)$$

From Equation (41), the CMOR end space position deviation ΔP is

$$\Delta P = P^R - P^N = B\Delta\eta \quad (42)$$

where $\Delta P = (\Delta x, \Delta y, \Delta z)^T$ is the CMOR end flange position error vector, P^R is the actual end flange position, P^N is the calculated end flange position, B is the parameter error identification Jacobi matrix, and $\Delta\eta$ is the parameter error vector of each joint, where $B = [J_\theta \ J_\alpha \ J_a \ J_d \ J_\beta]$, $\Delta\eta = [\Delta\theta \ \Delta\alpha \ \Delta a \ \Delta d \ \Delta\beta]^T$.

The CMOR varies its parameter errors in the joint space due to the flexibility of the link, the flexibility of the joint, the controller control error, the self-weight, and the load. With the change of the rotation angle in the joint space of the CMOR, the joint rotation angle produces a certain degree of error, but it is also accompanied by the link flexibility error, controller control error, and other parameters [40]. Therefore, each parameter error of CMOR can be expressed as a function of the joint angle

$$\Delta\eta = (\Delta\theta \ \Delta\alpha \ \Delta a \ \Delta d \ \Delta\beta) = f(\theta_1, \theta_2, \dots, \theta_8) \quad (43)$$

where $\Delta\eta$ denotes the set of parameter errors. It is difficult to model the errors in the joint space because the CMOR joints turning angles $\theta_1, \theta_2, \dots, \theta_8$ are coupled with each other. Therefore, the determined spatial poses in the CMOR joint space can be converted to the working space for solving

$$f(\theta_1, \theta_2, \dots, \theta_8) = g(x, y, z) \quad (44)$$

From Equations (43) and (44), it is known that given a set of positional parameters in joint space or workspace, the CMOR parameter error $\Delta\eta$ at that positional can be determined.

Due to the large variation of the CMOR end-effector position in the working space, the end-effector position error caused by non-geometric factors such as link flexibility, joint flexibility, controller control error, and self-weight in each spatial position is unevenly distributed. In addition, the end of the CMOR is under variable load from 0 to 2000 kg, which also has a large impact on the position accuracy of the end-effector. Therefore, the ability to compensate for the position error over the entire working space of the CMOR using a single fixed parameter error set $\Delta\eta$ is limited. In this paper, the variable parameter error compensation method using gridding of the CMOR workspace is shown in Figure 5. The smaller the individual meshes are divided the closer the CMOR is affected by non-geometric factors such as link flexibility, joint flexibility, controller control error, and self-weight. As a result, the absolute positioning accuracy of the end-effector in the whole working space is higher. By meshing the workspace and using the Levenberg-

Marquardt algorithm to sequentially identify the parameter error $\Delta\eta_i$ within each mesh, the absolute positioning accuracy of the CMOR end-effector in the entire workspace can be improved [41,42].

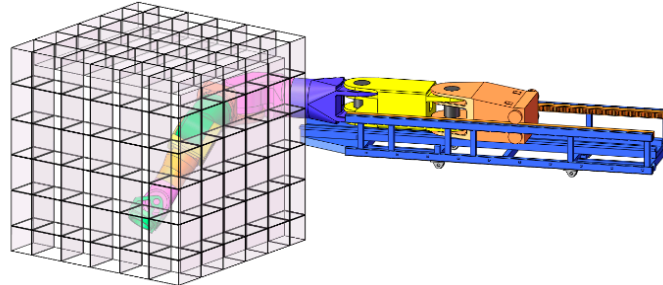


Figure 5. CMOR workspace gridding principle.

4. Simulation Validation

4.1. CMOR Rigid-Flexible Coupling Simulation System

To verify the accuracy of the ARSMC controller for the trajectory control of the CMOR rigid-flexible coupling model, the dynamics parameters of each joint and link are calculated based on the CMOR 3D model as shown in Table 2. Then the CMOR control system is built in MATLAB/Simulink environment. To realize the rigid-flexible coupling calculation, the CMOR 3D dynamics model is established in ADAMS software, and the CMOR rigid link is flexible using finite element software [43,44]. The co-simulation model is shown in Figure 6. Since the first two links of CMOR are made of stainless steel with less deformation, and the rest of the links are made of aluminium alloy with more deformation, only the aluminium alloy links are processed for rigid-flexible coupling. The modulus of elasticity of all aluminium alloy links is set to 70 Gpa and Poisson’s ratio is 0.3.

Table 2. The linkage dynamics parameters of CMOR.

Link i	Mass (kg)	Main Inertia (kg m ²)	Centre of Mass (m)
1	2739	3582	(0.895, 0, 0)
2	420	163	(0.37, 0, 0.074)
3	237	46	(−0.138, −0.064, 0.67)
4	181	77	(0.33, 0.308, 0.07)
5	168	16	(0, 0, 0.78)
6	331	99	(0, 0.426, 0.144)
7	61	4	(0, −0.089, 0.353)
8	167	19	(0.09, 0.211, 0.019)

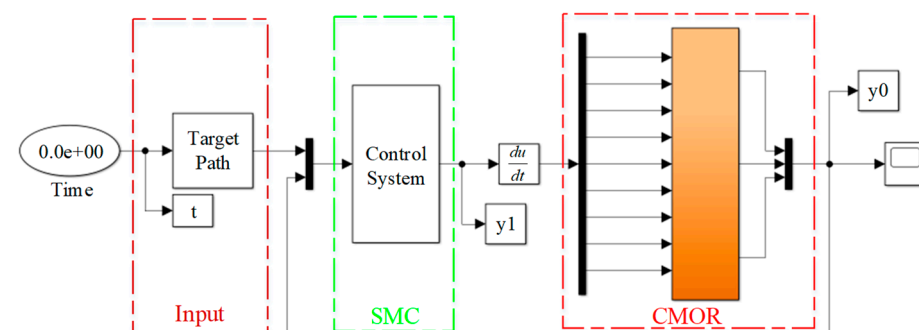


Figure 6. CMOR co-simulation program.

The static and dynamic friction coefficients of the CMOR joint are set to 0.5 and 0.3, respectively. CMOR joint 3 and later connecting rod are aluminium alloy material with a relatively small modulus of elasticity and large deformation, more prone to deformation

oscillation and other characteristics. And joints 3 and 4 are under the alternating torque, so given the target signal of joints 3 and 4 the rest of the joints remain stationary for dynamic characteristics and position accuracy analysis. The simulation takes into account the uncertainty of the model and external disturbance and sets the initial angle, angular velocity and angular acceleration of each joint to zero. The CMOR target trajectory is shown in Figure 7 for dynamic control and position error analysis.

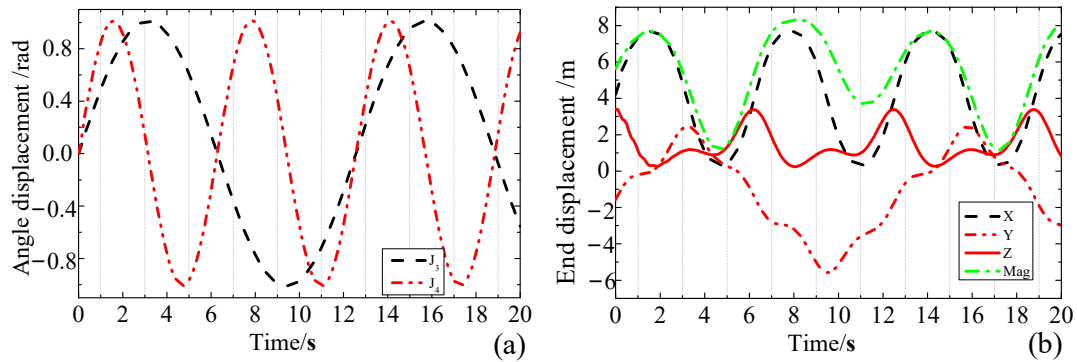


Figure 7. CMOR target trajectory (a) Joint Displacement (b) End Displacement.

4.2. CMOR Dynamic Control Effects

The load of the CMOR end-effector is set to 0 kg, 500 kg, 1000 kg and 2000 kg respectively, and the dynamic control of CMOR rigid-flexible model is carried out by ARSMC controller, and the control effect is shown in Figures 8–10. Simulation video and programmes are available in the Supplementary Materials. The dynamic response and position accuracy of CMOR under ARSMC controller in no-load condition are ideal. Under the no-load condition, the joint and link flexibility of CMOR has little influence on the position accuracy, and the sum of joint tracking error and flexible joint deformation error is around 0.01 rad with high tracking accuracy, and the maximum position error is less than 0.03 m.

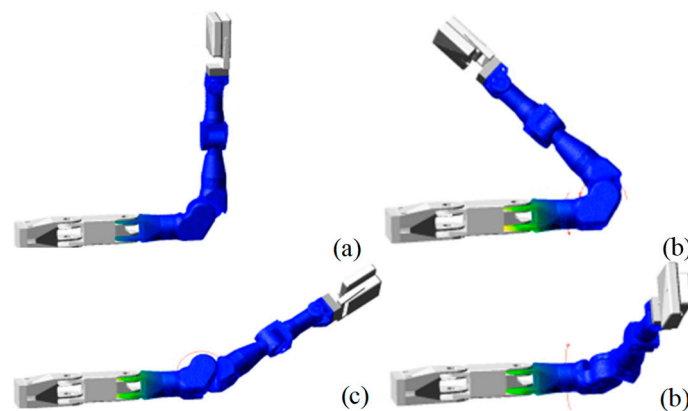


Figure 8. CMOR co-simulation motion timing diagram (a) Initial position of CMOR (b) Position of CMOR at 7 s (c) Position of CMOR at 15 s (d) Final position of CMOR.

When the load increases, both the joint angle error and the position error of the end-effector increase significantly. As the load increases the CMOR produces large oscillations in the starting phase, and after 4 s the CMOR reaches a steady state. The maximum angular error of CMOR in steady state is 0.023 rad and the maximum end position error is 0.3 m. This is mainly caused by the combined effect of rigid-flexible coupling deformation and control error of CMOR. At 5 s, 11 s and 17 s moments of the given joint drive signal, the CMOR moves to the cantilever state, and the end load tracking error and joint tracking error are in extreme values at these three points, which shows that the flexible deformation

of the cantilever state is the main reason for the end position accuracy. In general, the controller has good robustness with short convergence time and small tracking error, and high adaptability in the presence of external disturbances and uncertainties.

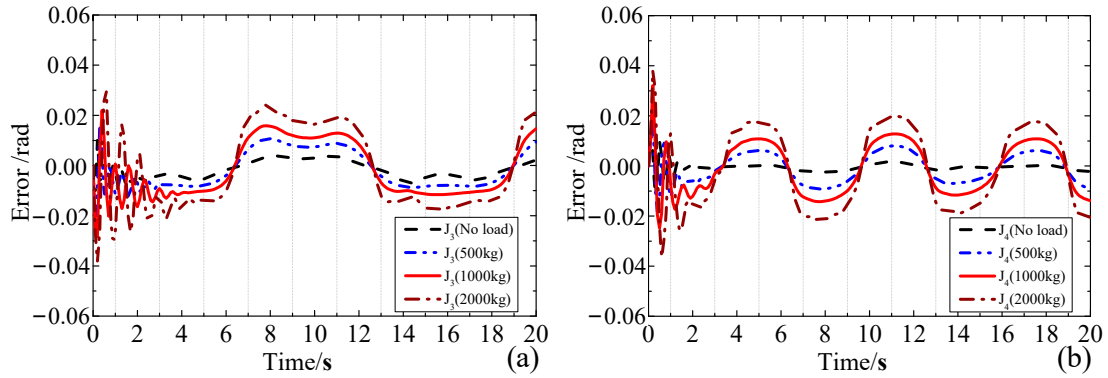


Figure 9. Position errors of J_3 joint and J_4 joint under different loads (a) Position errors of J_3 joint under different loads (b) Position errors of J_4 joint under different loads.

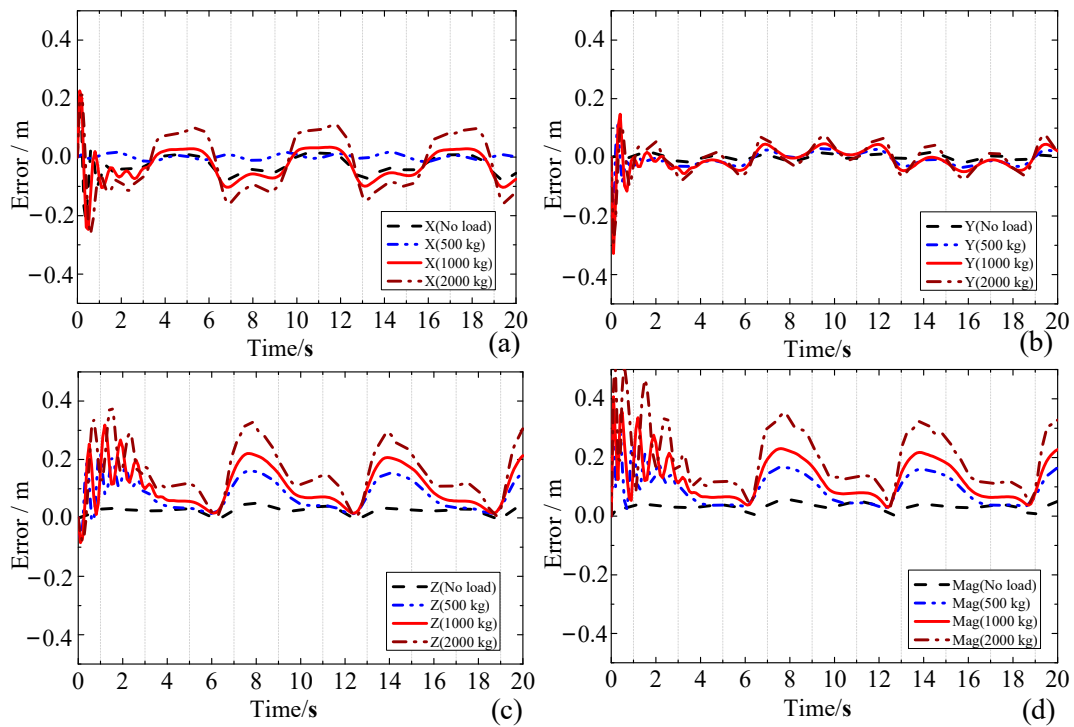


Figure 10. Position errors of CMOR end-effectors under different loads (a) Position error of X-axis under different loads (b) Position error of Y-axis under different loads (c) Position error of Z-axis under different loads (d) Absolute position error of CMOR under different loads.

4.3. CMOR Error Compensation Effects

To calculate the CMOR position error compensation effect, CMOR joint 3 is set to do sinusoidal motion as shown in Figure 11a, and CMOR can rotate left and right to the limit position. Set the end-effector with different loads (0–2000 kg) for ARSMC controller control performance simulation, and the results are shown in Figure 11b–d. The results show that the trajectory of joint angular error and position error in the simulation process is smooth and there is only damping oscillation at the beginning stage. The maximum tracking error of the joint angular displacement is less than 0.01 rad, and the maximum position error of the end-effector along the Z-axis is about 0.1 m. The absolute position

error of the end-effector is similar to the Z-axis position error, which shows that the position error of the end-effector mainly comes from the position error along the Z-axis caused by the self-weight of the CMOR flexible linkage and the end load.

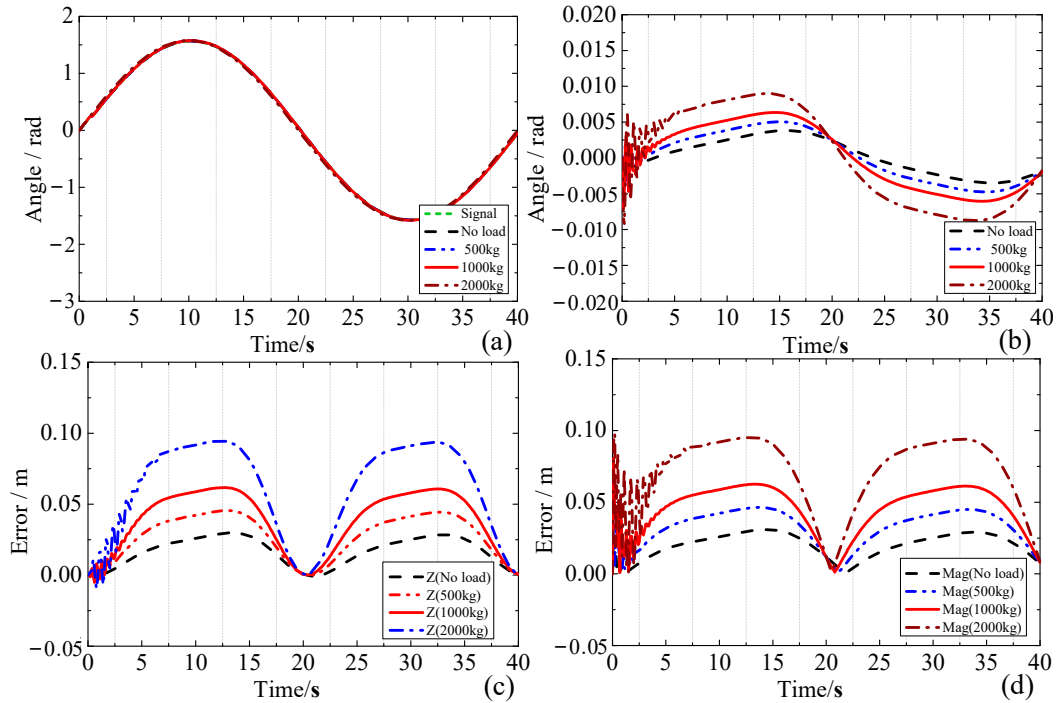


Figure 11. Dynamic response of J_3 joint motion under different loads (a) J_3 joint target trajectories (b) Rotation angle errors (c) Z-axis position errors (d) Absolute position errors.

The CMOR workspace is uniformly divided into 8 parts along the Y-axis of the base coordinate system, and the CMOR position error compensation method is used for variable parameter error compensation. The compensation parameters in each gridded workspace under different end loads are calculated by the parameter identification method as shown in Table 3. The compensation parameters are brought into the ARMRC controller and recalculated, and the results are shown in Figure 12. After compensation, the end position error of CMOR along the Z-axis is less than 0.02 m, and the mean value of absolute position error is less than 0.025 m, which reduces the end position error by more than 4 times with obvious compensation effect. Figure 12b in the 0 s and 20 s position error is large, mainly due to the large variation of error values in this region and the sparse gridded workspace. The grid can be further refined to improve the position accuracy.

Table 3. Compensation value at the corresponding spatial position of J_3 joint (rad).

Location	1	2	3	4	5	6	7	8
Load (2000 kg)	-1.278×10^{-2}	-1.845×10^{-2}	-1.989×10^{-2}	-1.601×10^{-2}	1.2377×10^{-2}	1.824×10^{-2}	1.9677×10^{-2}	1.5654×10^{-2}
Load (1000 kg)	-7.5639×10^{-3}	-1.1553×10^{-2}	-1.2997×10^{-2}	-1.0945×10^{-2}	7.1556×10^{-3}	1.1316×10^{-2}	1.2758×10^{-2}	1.0448×10^{-2}
Load (500 kg)	-5.1178×10^{-3}	-8.1092×10^{-3}	-9.5541×10^{-3}	-8.4212×10^{-3}	4.5582×10^{-3}	7.8585×10^{-3}	9.3027×10^{-3}	7.8615×10^{-3}
No load	-2.6475×10^{-3}	-4.7373×10^{-3}	-6.1861×10^{-3}	-5.9613×10^{-3}	2.0227×10^{-3}	4.4708×10^{-3}	5.9173×10^{-3}	5.3341×10^{-3}

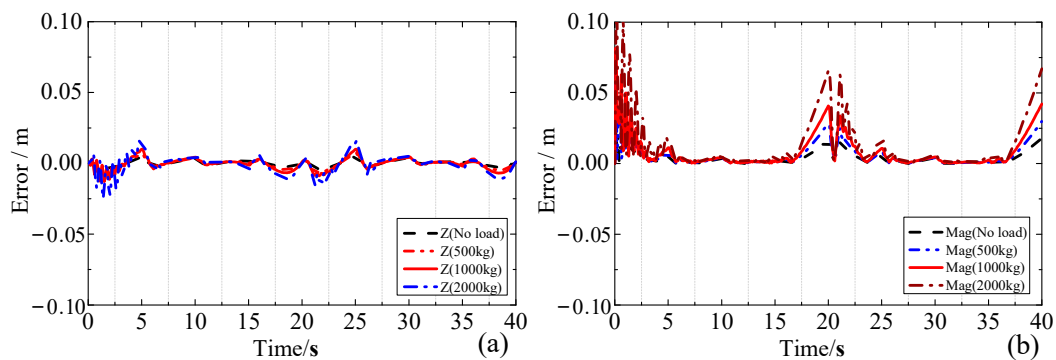


Figure 12. CMOR position error compensation results (a) Z-axis end position error of CMOR (b) End space position error of CMOR.

5. Conclusions

This paper establishes the kinematic and dynamic models based on the structural characteristics of CMOR using the improved DH parameter method and Lagrangian method, respectively, and analyzes the working process in the vacuum chamber. The influence of non-geometric factors such as long cantilevers (9 m), large loads (2.5 tons), and flexibility between joints and links makes CMOR dynamic control very difficult. To address the complex nonlinearity and rigid-flexible coupling uncertainty of the CMOR dynamics model, a CMOR adaptive robust sliding mode controller (ARSMC) is designed based on the Hamilton-Jacobi equation for dynamic control to improve the robustness of the control system. An error compensation method is proposed to compensate for the effects of non-geometric factors such as the flexibility between the CMOR joints and the links on the position accuracy. Based on the matrix differentiation method and gridded workspace principle, the CMOR coupling parameter errors are decoupled to realize the error compensation of the whole workspace and improve the motion control accuracy. Since CMOR is still under development, so the prototype test results of CMOR are not available at this time. Therefore, the CMOR rigid-flexible coupling simulation system is established by ADAMS-MATLAB/Simulink to analyze the dynamic control effect of ARSMC. The simulation results show that the maximum position error of the CMOR end-effector under the composite motion process is more than 0.3 m, and the end position error of single joint motion is also more than 0.1 m. Parameter identification and compensation can be performed by matrix differentiation method and gridded workspace principle, and the average position error after compensation is less than 0.025 m, and the absolute error value is reduced by 4 times. The large position errors at 0 s and 20 s are mainly caused by the large variation of error values in this region and the sparse gridded workspace. The position accuracy can be further improved by increasing the grid density.

In the future, we will continue to develop CMOR control strategies and prototype manufacturing work. The effectiveness of the precise control strategy is further verified by designing the CMOR motion planning method for motion planning and dynamic control of specific tasks in the vacuum chamber.

Supplementary Materials: The following supporting information can be downloaded at: <https://www.mdpi.com/article/10.3390/app131810487/s1> and https://youtu.be/IQxoUkS_XPI (accessed on 17 September 2023).

Author Contributions: Conceptualization, C.Z. and G.Q.; Data curation, C.Z.; Formal analysis, L.L., R.Z. and W.W.; Funding acquisition, C.Z. and Y.C.; Investigation, H.P. and W.W.; Methodology, L.X. and W.W.; Project administration, G.L.; Resources, C.Z. and C.W.; Supervision, W.W.; Validation, C.Z.; Visualization, C.Z., F.W., P.Z., X.Q. and N.S.; Writing—original draft, C.Z. and G.Q. All authors have read and agreed to the published version of the manuscript.

Funding: This work is supported by the National Natural Science Foundation of China (Grant Nos. 12305251 and 11905147) and the Comprehensive Research Facility for Fusion Technology Program of China (Contract No. 2018-000052-73-01-001228).

Institutional Review Board Statement: Not applicable.

Informed Consent Statement: Not applicable.

Data Availability Statement: The data and code used to support the findings of this study are available from the corresponding authors upon request (congju_zuo@126.com; gdqin@ipp.ac.cn).

Conflicts of Interest: The authors declare no conflict of interest.

References

1. Toschi, R. Nuclear fusion, an energy source. *Fusion Eng. Des.* **1997**, *36*, 1–8. [[CrossRef](#)]
2. Kessel, C.E.; Blanchard, J.P.; Davis, A.; El-Guebaly, L.; Ghoniem, N.; Humrickhouse, P.W.; Malang, S.; Merrill, B.J.; Morley, N.B.; Neilson, G.H.; et al. The fusion nuclear science facility, the critical step in the pathway to fusion energy. *Fusion Sci. Technol.* **2015**, *68*, 225–236. [[CrossRef](#)]
3. Zhao, Z.; Zhang, L.; Zhou, R.; Yang, Y.; Zhang, W.; Cheng, Y.; Morita, S.; Ti, A.; Hu, A.; Sun, Z.; et al. Impurity Behavior in Plasma Recovery after a Vacuum Failure in the Experimental Advanced Superconducting Tokamak. *Appl. Sci.* **2023**, *13*, 4338. [[CrossRef](#)]
4. Wan, Y.; Li, J.; Liu, Y.; Wang, X.; Chan, V.; Chen, C.; Duan, X.; Fu, P.; Gao, X.; Feng, K.; et al. Overview of the present progress and activities on the CFETR. *Nucl. Fusion* **2017**, *57*, 102009. [[CrossRef](#)]
5. Ribeiro, I.; Damiani, C.; Tesini, A.; Kakudate, S.; Siuko, M.; Neri, C. The remote handling systems for ITER. *Fusion Eng. Des.* **2011**, *86*, 471–477. [[CrossRef](#)]
6. Cheng, Y.; Song, Y.; Wu, H.; Yang, Y.; Zhang, J.; Pan, H.; Zhao, W.; Zhou, N.; Tang, Y.; Zhang, Y.; et al. Overview of the CFETR remote handling system and the development progress. *Fusion Eng. Des.* **2022**, *177*, 113060. [[CrossRef](#)]
7. Aymerich, E.; Cannas, B.; Pisano, F.; Sias, G.; Sozzi, C.; Stuart, C.; Carvalho, P.; Fanni, A.; JET Contributors. Performance Comparison of Machine Learning Disruption Predictors at JET. *Appl. Sci.* **2023**, *13*, 2006. [[CrossRef](#)]
8. Qin, G.; Ji, A.; Wang, W.; Zhao, W.; Pan, H.; Cheng, Y.; Song, Y. Analyzing trajectory tracking accuracy of a flexible multi-purpose deployer. *Fusion Eng. Des.* **2020**, *151*, 111396. [[CrossRef](#)]
9. Qin, G.; Ji, A.; Cheng, Y.; Zhao, W.; Pan, H.; Shi, S.; Song, Y. Position error compensation of the multi-purpose overload robot in nuclear power plants. *Nucl. Eng. Technol.* **2021**, *53*, 2708–2715. [[CrossRef](#)]
10. Jin, L.; Zhang, Y. G2-type SRMPC scheme for synchronous manipulation of two redundant robot arms. *IEEE Trans. Cybern.* **2014**, *45*, 153–164.
11. Zhang, H.; Jin, H.; Liu, Z.; Liu, Y.; Zhu, Y.; Zhao, J. Real-time kinematic control for redundant manipulators in a time-varying environment: Multiple-dynamic obstacle avoidance and fast tracking of a moving object. *IEEE Trans. Ind. Inform.* **2019**, *16*, 28–41. [[CrossRef](#)]
12. Liu, Q.; Huang, T. Inverse kinematics of a 5-axis hybrid robot with non-singular tool path generation. *Robot. Comput.-Integr. Manuf.* **2019**, *56*, 140–148. [[CrossRef](#)]
13. Manuelraj, M.S.; Dutta, P.; Gotewal, K.K.; Rastogi, N.; Tesini, A.; Choi, C.H. Structural analysis of ITER multipurpose deployer. *Fusion Eng. Des.* **2016**, *109*, 1296–1301. [[CrossRef](#)]
14. Cibicik, A.; Pedersen, E.; Egeland, O. Dynamics of luffing motion of a flexible knuckle boom crane actuated by hydraulic cylinders. *Mech. Mach. Theory* **2020**, *43*, 103616. [[CrossRef](#)]
15. Anderson, K.S.; Crichtley, J.H. Improved Order- N' performance algorithm for the simulation of constrained multi-rigid-body dynamic systems. *Multibody Syst. Dyn.* **2003**, *9*, 185–212. [[CrossRef](#)]
16. Dwivedy, S.K.; Eberhard, P. Dynamic analysis of flexible manipulators, a literature review. *Mech. Mach. Theory* **2006**, *41*, 749–777. [[CrossRef](#)]
17. Martins, J.M.; Mohamed, Z.; Tokhi, M.O.; Da Costa, J.S.; Botto, M.A. Approaches for dynamic modelling of flexible manipulator systems. *IEE Proc.-Control Theory Appl.* **2003**, *150*, 401–411. [[CrossRef](#)]
18. Al-Bedoor, B.O.; Almusallam, A.A. Dynamics of flexible-link and flexible-joint manipulator carrying a payload with rotary inertia. *Mech. Mach. Theory* **2000**, *35*, 785–820. [[CrossRef](#)]
19. Al-Bedoor, B.O.; Khulief, Y.A. Finite element dynamic modeling of a translating and rotating flexible link. *Comput. Methods Appl. Mech. Eng.* **1996**, *131*, 173–189. [[CrossRef](#)]
20. Subudhi, B.; Morris, A.S. Dynamic modelling, simulation and control of a manipulator with flexible links and joints. *Robot. Auton. Syst.* **2002**, *41*, 257–270. [[CrossRef](#)]
21. Zhu, G.; Ge, S.S.; Lee, T.H. Simulation studies of tip tracking control of a single-link flexible robot based on a lumped model. *Robotica* **1999**, *17*, 71–78. [[CrossRef](#)]
22. Braganza, D.; Dawson, D.M.; Walker, I.D.; Nath, N. A neural network controller for continuum robots. *IEEE Trans. Robot.* **2007**, *23*, 1270–1277. [[CrossRef](#)]
23. Racioppo, P.; Ben-Tzvi, P. Design and control of a cable-driven articulated modular snake robot. *IEEE/ASME Trans. Mechatron.* **2019**, *24*, 893–901. [[CrossRef](#)]

24. Goldman, R.E.; Bajo, A.; Simaan, N. Compliant motion control for multisegment continuum robots with actuation force sensing. *IEEE Trans. Robot.* **2014**, *30*, 890–902. [[CrossRef](#)]
25. Ider, S.K. Force and motion trajectory tracking control of flexible-joint robots. *Mech. Mach. Theory* **2000**, *35*, 363–378. [[CrossRef](#)]
26. Khalil, W.; Besnard, S. Geometric calibration of robots with flexible joints and links. *J. Intell. Robot. Syst.* **2002**, *34*, 357–379. [[CrossRef](#)]
27. Wang, D.; He, H.; Liu, D. Adaptive critic nonlinear robust control: A survey. *IEEE Trans. Cybern.* **2017**, *47*, 3429–3451. [[CrossRef](#)] [[PubMed](#)]
28. Ullah, S.; Mehmood, A.; Khan, Q.; Rehman, S.; Iqbal, J. Robust integral sliding mode control design for stability enhancement of under-actuated quadcopter. *Int. J. Control Autom. Syst.* **2020**, *18*, 1671–1678. [[CrossRef](#)]
29. Roy, S.; Roy, S.B.; Lee, J.; Baldi, S. Overcoming the underestimation and overestimation problems in adaptive sliding mode control. *IEEE/ASME Trans. Mechatron.* **2019**, *24*, 2031–2039. [[CrossRef](#)]
30. Li, B.; Tian, W.; Zhang, C.; Hua, F.; Cui, G.; Li, Y. Positioning error compensation of an industrial robot using neural networks and experimental study. *Chin. J. Aeronaut.* **2021**, *35*, 346–360. [[CrossRef](#)]
31. Le, P.N.; Kang, H.J. A Robotic Calibration Method Using a Model-Based Identification Technique and an Invasive Weed Optimization Neural Network Compensator. *Appl. Sci.* **2020**, *10*, 7320. [[CrossRef](#)]
32. Ni, H.; Zhang, C.; Hu, T.; Wang, T.; Chen, Q.; Chen, C. A dynamic parameter identification method of industrial robots considering joint elasticity. *Int. J. Adv. Robot. Syst.* **2019**, *16*, 1729881418825217. [[CrossRef](#)]
33. Chen, D.; Wang, T.; Yuan, P.; Sun, N.; Tang, H. A positional error compensation method for industrial robots combining error similarity and radial basis function neural network. *Meas. Sci. Technol.* **2019**, *30*, 125010. [[CrossRef](#)]
34. Zhou, J.; Kang, H.J. A hybrid least-squares genetic algorithm-based algorithm for simultaneous identification of geometric and compliance errors in industrial robots. *Adv. Mech. Eng.* **2015**, *7*, 1687814015590289. [[CrossRef](#)]
35. Zhang, Q.; Song, B.; Cai, B.; Sun, Y. Design of Coordination System for Composite Mobile Robot Platform Oriented to Nuclear Fusion Vessel. *J. Fusion Energy* **2021**, *40*, 22. [[CrossRef](#)]
36. Van Der Schaft, A.J. L sub 2-gain analysis of nonlinear systems and nonlinear state-feedback H-sub infinity control. *IEEE Trans. Autom. Control* **1992**, *37*, 770–784. [[CrossRef](#)]
37. Wang, Y.; Sun, W.; Xiang, Y.; Miao, S. Neural network-based robust tracking control for robots. *Intell. Autom. Soft Comput.* **2009**, *15*, 211–222. [[CrossRef](#)]
38. Niu, B.; Zhao, J. Stabilization and L2-gain analysis for a class of cascade switched nonlinear systems: An average dwell-time method. *Nonlinear Anal. Hybrid Syst.* **2011**, *5*, 671–680. [[CrossRef](#)]
39. Hayati, S.A. Robot arm geometric link parameter estimation. In Proceedings of the 22nd IEEE Conference on Decision and Control, San Antonio, TX, USA, 14–16 December 1983; pp. 1477–1483.
40. Hong, P.; Tian, W.; Mei, D.; Zeng, Y.F. Robotic variable parameter accuracy compensation using space grid. *Robot* **2015**, *37*, 327–335.
41. Luo, G.; Zou, L.; Wang, Z.; Lv, C.; Ou, J.; Huang, Y. A novel kinematic parameters calibration method for industrial robot based on Levenberg-Marquardt and Differential Evolution hybrid algorithm. *Robot. Comput.-Integr. Manuf.* **2021**, *71*, 102165. [[CrossRef](#)]
42. Shawash, J.; Selviah, D.R. Real-time nonlinear parameter estimation using the Levenberg–Marquardt algorithm on field programmable gate arrays. *IEEE Trans. Ind. Electron.* **2012**, *60*, 170–176. [[CrossRef](#)]
43. Zhang, C.; Yu, Y. Dynamic modeling of robot arm with joint and link flexibility manipulating a constrained object. *Chin. J. Mech. Eng.* **2003**, *39*, 9–12. [[CrossRef](#)]
44. Liu, N.; Zhang, X.; Zhang, L.; Shang, D.; Fan, X. Study on the Rigid-Flexible Coupling Dynamics of Welding Robot. *Wirel. Pers. Commun.* **2018**, *102*, 1683–1694. [[CrossRef](#)]

Disclaimer/Publisher’s Note: The statements, opinions and data contained in all publications are solely those of the individual author(s) and contributor(s) and not of MDPI and/or the editor(s). MDPI and/or the editor(s) disclaim responsibility for any injury to people or property resulting from any ideas, methods, instructions or products referred to in the content.